



Title	Projected sea level rise, gyre circulation and water mass formation in the western North Pacific: CMIP5 inter-model analysis
Author(s)	Terada, Mio; Minobe, Shoshiro
Citation	Climate dynamics, 50(11-12), 4767-4782 https://doi.org/10.1007/s00382-017-3902-8
Issue Date	2018-06
Doc URL	http://hdl.handle.net/2115/74531
Rights	The final publication is available at link.springer.com
Type	article (author version)
File Information	Terada_Minobe_2018_CD_SLR_final.pdf



[Instructions for use](#)

Projected sea level rise, gyre circulation and water mass formation in the western North Pacific:

CMIP5 inter-model analysis

Mio Terada¹ and Shoshiro Minobe^{1,2}

¹ Natural History Sciences, Graduate School of Science, Hokkaido University, Sapporo, Japan

² Earth and Planetary Sciences, Faculty of Science, Hokkaido University, Sapporo, Japan

Corresponding author:

Mio Terada

E-mail: mio.terada@sci.hokudai.ac.jp

Tel.: +81-11-706-4676

Address: Room 302, Rigaku Building No. 8, Faculty of Science,

Hokkaido University, Sapporo, N10, W8, 060-0810, Japan

Keywords: dynamic sea level; CMIP5 climate models; western North Pacific; Kuroshio Extension;

subtropical mode water; global warming

1 Abstract

2 Future changes in the dynamic sea level (DSL), which is defined as sea-level deviation from
3 the global mean sea level, is investigated over the North Pacific, by analyzing data from the Coupled
4 Model Intercomparison Project Phase 5 (CMIP5). The analysis provides more comprehensive
5 descriptions of DSL responses to the global warming in this region than available from previous studies,
6 by using surface and subsurface data until the year 2300 under middle and high greenhouse-gas emission
7 scenarios. The DSL changes in the North Pacific are characterized by a DSL rise in the western North
8 Pacific around the Kuroshio Extension (KE), as also reported by previous studies. Subsurface density
9 analysis indicates that DSL rise around the KE is associated with decrease in density of subtropical mode
10 water (STMW) and with northward KE migration, the former (latter) of which is relatively strong
11 between 2000 and 2100 for both RCP4.5 and RCP8.5 (between 2100 and 2300 for RCP8.5). The STMW
12 density decrease is related to large heat uptake to the south and southeast of Japan, while the northward
13 KE migration is associated with the poleward shift of the wind stress field. These features are commonly
14 found in multi-model ensemble means and the relations among representative quantities produced by
15 different climate models.

16

17

18

19 1. Introduction

20 Sea-level rise due to global warming is an important issue for human society (see, among others,
21 Lowe and Gregory 2006; Nicholls et al. 2014; Timmermann et al. 2010; Willis and Church 2012). In the
22 Fifth Assessment Report of the Intergovernmental Panel on Climate Change (IPCC-AR5), the future
23 global mean sea-level rise in the 2081–2100 period, relative to the 1986–2005 period, is estimated as
24 0.47m (0.32–
25 0.63m of 90% likely range) and 0.63m (0.45-0.82m of 90% likely range) for the middle and high
26 greenhouse-gas emission scenarios in Representative Concentration Pathways (RCP) 4.5 and RCP8.5,
27 respectively (Church et al. 2013). An updated assessment by Slangen et al. (2014) suggested higher
28 values: 0.54 m for RCP4.5 and 0.71 m for RCP8.5. Because of continued ocean warming and further
29 melting of the Greenland ice sheet, the global mean sea-level rise continues even when greenhouse-gas
30 concentration is stabilized (Church et al. 2013).

31 Sea-level rise can be expressed as the sum of the global mean sea-level and a regional sea-level
32 correction defined by the deviation of sea level in the region from the global mean. Regional sea-level
33 change is characterized by the gravity adjustment of land-ice melt (Slangen et al. 2014), terrestrial water
34 storage changes resulting from groundwater depletion (Wada et al. 2012), uplifting of the solid earth due
35 to land-ice mass change (Mitrovica et al. 2011), long term glacial isostatic adjustment (Peltier 2004),
36 non-uniform heat uptake by the ocean (e.g., Lowe and Gregory 2006; Suzuki and Ishii 2011b), and

37 variation of ocean circulation (e.g., Gregory et al. 2001; Yin et al. 2010). Among these components, the
38 last two involve complex dynamic and thermodynamic responses of the ocean to atmospheric forcing, and
39 the difference in sea-level relative to the global mean attributable to these components is called the
40 dynamic sea level (hereinafter, DSL) (e.g., Yin et al. 2010; Zhang et al. 2014). Better understanding of
41 DSL for individual basins is needed for better understanding of sea-level rise issues. In this paper, we
42 study future changes in DSL due to ocean properties (i.e. non-uniform heat uptake and variation of ocean
43 circulation) for the North Pacific.

44 DSL change over the North Pacific due to global warming is characterized by relatively large
45 sea-level rise in the western North Pacific to the east of Japan. This feature is commonly found in the
46 multi-model ensemble (MME) mean of CMIP3 (Pardaens et al. 2010; Yin et al. 2010; Sueyoshi and
47 Yasuda 2012; Zhang et al. 2014) as well as that of CMIP5 (Yin 2012; Church et al. 2013; Slangen et al.
48 2014). Since the location of the localized sea-level rise roughly corresponds to the Kuroshio and the
49 Kuroshio Extension (KE), most previous studies have suggested that the rise is related to these currents
50 (Yin et al. 2010; Sueyoshi and Yasuda 2012; Zhang et al. 2014; Liu et al. 2016). Analyzing multiple
51 models of CMIP3, Sueyoshi and Yasuda (2012) reported that the meridional migration and strengthening
52 of the KE each contribute to the regional sea-level change, but these two modes of the KE change occur
53 differently in different models. The northward migration of the KE is associated with the northward shift
54 of the latitude of zero Sverdrup stream function (SSF), which gives the boundary between the subtropical

55 and subpolar gyres of wind-stress-forced circulations in linear models. This is consistent with another
56 CMIP3 analysis by Zhang et al. (2014) and downscaling of three CMIP5 models by Liu et al. (2016). The
57 poleward shift of the zero-SSF line is closely associated with the northward move of the Aleutian Low
58 (Sueyoshi and Yasuda 2012), and is probably related to the northward expansion of the mean atmospheric
59 circulation, including the Hadley cell (Miller et al. 2006, Rauthe et al. 2004, Collins et al. 2013).

60 In addition to wind forcings, anomalous heat flux to the ocean can be important in localized
61 sea-level rise in the western North Pacific. Using a series of experiments with a climate model, Suzuki
62 and Ishii (2011a) suggested that large heat uptake, via surface heat flux, in the subtropical mode water
63 (STMW) lowers density of that water mass, resulting in a larger sea-level rise over it. This explanation is
64 consistent with an earlier modeling experiment by Lowe and Gregory (2006). Furthermore, Suzuki and
65 Ishii (2011b) reported that warming and freshening of STMW has played an important role in sea-level
66 rise around the subtropical gyre in the North Pacific over the last three decades by using gridded
67 temperature and salinity data from Ishii and Kimoto (2009).

68 Further studies are important to better understanding of future DSL changes over the North Pacific.
69 The potential role of heat uptake of STMW has not been investigated in previous multi-model analyses.
70 Moreover, few previous studies of DSL change over the North Pacific using multi-model data of CMIP3
71 or CMIP5 have analyzed the differences among models. The study by Sueyoshi and Yasuda (2012) is a
72 notable exception, but that analysis is limited to only the 21st century under the middle scenario of the

73 IPCC Special Report on Emission Scenarios (SRES) A1B and does not consider subsurface density and
74 velocity fields. Therefore, expanding analysis to multiple scenarios and to a longer time duration (up to the
75 23rd century, for which some of CMIP models are available) and including subsurface density and
76 velocity fields will clearly advance understanding of sea-level rise. Toward that end, the purpose of this
77 study is to provide a more comprehensive description and an improved mechanism for assessment of
78 future DSL changes over the North Pacific by analyzing model dependency using multiple climate
79 models of CMIP5. In this study, we analyze both the middle scenario (RCP4.5) and the high scenario
80 (RCP8.5) until the 23rd century, using the outputs of more than 30 climate models for the 21st century.
81 This is more than double the 15 models used by Sueyoshi and Yasuda (2012) the 11 models used by
82 Zhang et al. (2014).

83 The rest of the paper is organized as follows. Section 2 describes the climate models and method
84 used in this study. Section 3 examines DSL change and the associated change of density and velocity in
85 the subsurface ocean. Section 4 analyzes how DSL changes are related to surface forcings. Section 5
86 presents a discussion and summary.

87

88 2. Data and Methods

89 The outputs used in this study, which come from climate models participating in CMIP5 (Taylor et al.
90 2012), are obtained mainly through the Program for Climate Model Diagnosis and Intercomparison

91 (<http://cmip-pcmdi.llnl.gov/cmip5/>). We used model outputs for the historical experiment up to December
92 2005 and those for the high- and medium-emissions scenarios of RCP8.5 and RCP4.5, respectively, for
93 January 2006 to December 2300. Outputs of RCP2.6 and RCP6.0 are not analyzed in this study because
94 of the relatively smaller number of available models. Green-house gas concentration and thus radiative
95 forcing stabilizes shortly after 2100 in RCP4.5 (Thomson et al. 2011), and in 2240 in RCP8.5 (Liddicoat
96 et al. 2012). We used outputs of 34 (32) models for RCP8.5 (RCP4.5) until 2100 and of 6 models until
97 2300. Heat flux data (*hfds* from CMIP5) are available to the authors from the 23 (9) listed models for
98 RCP8.5 (RCP4.5). We used only the first ensemble of each model so as to treat all models equally. All
99 model outputs are interpolated to a common horizontal grid with $1^\circ \times 1^\circ$ resolution for estimating the
100 MME, and the three-dimensional temperature and salinity data are also interpolated to a common set of
101 28 vertical levels.

102 The DSL was defined as the sea level relative to the global mean sea level of CMIP5 models (*zos*
103 from CMIP5). As mentioned above, DSL includes neither glacial isostatic adjustment nor gravitational
104 adjustment of land-ice melt and change in land water storage. The inverted barometer effect is not
105 considered because the DSL change related to atmospheric pressure change is much smaller than the
106 steric and DSL change (Slangen et al. 2014).

107 To understand how sea-level changes are related to density changes at depth, the contribution of the
108 steric component to DSL change is estimated. Sea level can be generally decomposed into steric and mass

109 components (Yin et al. 2010; Zhang et al. 2014; Liu et al. 2016). The sea-level differences due to the
 110 steric effect between two epochs ($\Delta\eta$) is given by using the hydrostatic balance:

$$\Delta\eta = -\frac{1}{\rho_0} \int_{h_{REF}}^0 \Delta\rho dz, \quad (1)$$

111 where $\Delta\rho$ is the in-situ density difference, h_{REF} is the reference depth and ρ_0 is the reference density.
 112 The reference depth is set to 2000 m, and the reference density is set to 1025 kg/m³. To understand the
 113 density changes corresponding to DSL, we introduce local density, which is defined by the density
 114 relative to the global mean density at each depth. This approach allows us to examine how DSL is related
 115 to the three-dimensional density structure at each depth in more detail than allowed by the approach
 116 employed by Yin et al. (2010), who defined local steric sea-level rise after calculating steric sea-level by
 117 vertical integration of densities.

118 We also calculate the geostrophic velocities using in-situ densities, calculated from temperature and
 119 salinity, and sea surface heights on a 1° × 1° grid. Surface velocities are obtained from sea surface height
 120 with geostrophic balance assumption, and subsurface velocities are calculated by integrating the thermal
 121 wind equation from the surface to downward without an assumption of a level of no motion. It is
 122 noteworthy that publicly available CMIP5 data have velocity components only in the original coordinate
 123 system of the model, without information on the angles of coordinates relative to the meridian. This
 124 makes it difficult to obtain zonal and meridional components of velocities from CMIP5 outputs by
 125 coordinate rotation. Despite this, by using geostrophic velocities, we can assess changes in subsurface

126 oceanic circulation.

127

128 3. DSL and Density Changes

129 The spatial structure of DSL changes differs before and after 2100. Until 2100, changes are
130 characterized by a meridional dipole accompanying DSL rises (falls) in the subtropical (subpolar) gyre in
131 the western North Pacific for both the RCP4.5 and RCP8.5 scenarios (Figs. 1a and 1b). This is consistent
132 with previous studies using CMIP5 models (Yin 2012; Church et al. 2013; Slangen et al. 2014) and
133 CMIP3 models (e.g., Sueyoshi and Yasuda 2012; Zhang et al. 2014). These patterns are somewhat
134 (completely) different from the DSL change pattern for RCP8.5 (RCP4.5) from 2100 to 2300. For
135 RCP8.5, the strong DSL rise to the east of Japan between 2100 and 2300 is shifted northward from that
136 between 2000 and 2100, exhibiting a monopole pattern over the basin (Fig. 1c). The maximal DSL rise
137 between the 20th and 21st centuries is 11 cm, occurring near the KE east of Japan, and is 23 cm between
138 the 21st and 23rd centuries for RCP8.5. In contrast, DSL changes after 2100 for RCP4.5 are very weak
139 around the KE, and slightly positive in the eastern and northern North Pacific (Fig. 1d). The changed
140 structure before and after 2100 is not due to different ensemble sizes (30+ vs 6): the pattern of DSL
141 changes before 2100 identified from the MME of six models that are available through the 23rd century is
142 essentially the same as found with a larger number of models used to produce Figs. 1a and 1b (Figs. 1e
143 and 1f).

144 Time series of area-averaged DSL anomaly from the 1971-2000 mean around the KE over 30°–

145 45°N and 145°–170°E are generally consistent with the temporal evolution of radiative forcing in each
146 scenario. The time series from RCP8.5 exhibits faster and longer lasting increases than seen from RCP4.5
147 (Fig. 2). The DSL anomaly is rather stable during the end of the 20th century and the early 21st century,
148 and then starts increasing before 2050 for both scenarios. These results for 30+ models are statistically
149 robust, because the 5-95% likely range of 30-year mean MME DSL for each periods are smaller than \pm
150 10% of its value. The area-averaged DSL anomaly appears to continuously increase until around the end
151 of the 21st century for RCP4.5 and until the end of the 23rd century for RCP8.5, but internal variability
152 from individual model is remained in 6-model MMEs because of the small ensemble size. Since DSL
153 change in RCP4.5 is weak after 2100, we analyze RCP4.5 only before 2100.

154 The DSL changes shown in Fig. 1 are quite well explained by the steric component (Fig. 3).
155 Thus, the DSL change over the North Pacific is dominated by the steric sea-level change. This is
156 consistent with the findings of Yin et al. (2010), who showed that the steric component is dominant in the
157 open ocean. To better understand how three-dimensional density changes are related to DSL changes, we
158 examine local density, which is defined as the density relative to the global mean density at each depth, as
159 mentioned in Section 2 (Fig. 4). We focus our attention to DSL changes east of Japan, where large DSL
160 changes are found until 2100 under both scenarios and until 2300 in the RCP8.5 scenario, as shown in Fig.
161 1. Until 2100, the local density decrease is centered around 30°N between depths of 100 and 300 m (Figs.
162 4a and 4c). In this region, the climatological vertical density gradient is weak, as shown by the wider

163 distance between the σ (1000 kg/m^3 is subtracted from in-situ density) contours of 25 and 27 kg/m^3 for the
164 end of the 20th century, indicating the presence of STMW. This means that the decreases in local density
165 occur in the STMW, locating over the southern flank of KE and further south. In contrast, after 2100, the
166 local density decrease has its maximum around 39°N , corresponding to the KE axis rather in the STMW
167 region (Fig. 4b). The large negative change in local density near the KE axis suggests its northward
168 migration. Although the density decreases in the region of STMW and near the KE axis occur in both the
169 21st and 22nd–23rd centuries, the density decreases more strongly in the region of STMW than around
170 the KE axis until 2100 under both RCP4.5 and RCP8.5. Furthermore, the density decreases more strongly
171 around the KE axis than in the STMW region after 2100 under RCP8.5. The density decrease in the
172 STMW is accompanied by a temperature increase (not shown), which suggests that heat uptake associated
173 with the STMW plays an important role in DSL change, as suggested by Suzuki and Ishii (2011b). It is
174 interesting to note that Sugimoto et al. (2017) very recently reported that an enhanced warming of the
175 STMW under the global warming may have already occurred over the past six decades.

176 The MME time series of volume-averaged local density anomaly for the STMW and for the
177 KE axis latitude anomaly exhibit negative and positive trends, respectively (Fig. 5). The KE axis latitude
178 is estimated as the center of gravity of eastward geostrophic surface velocity, zonally averaged over 145° –
179 170°E , 25° – 50°N with westward velocities being ignored. Before the 2000s, the time series of STMW
180 density anomaly is roughly stable, but the KE axis latitude appears to start migrating northward before

181 2000.

182 Next, we investigate whether these relations we found in MME are common for all models, and
183 if so, we determine how strongly each variables can explain the DSL differences among models. Figure 6
184 shows the relation between DSL changes resulting from changes in STMW density and the DSL changes
185 generally in the region of STMW. The regression slopes are close to unity (1.54 and 1.45 for RCP8.5 and
186 RCP4.5, respectively for 30+ models), and the correlations are strong ($r=0.63-0.83$), indicating that the
187 local decrease of density in the STMW well explains the DSL rise there for both periods and scenarios.
188 Figure 7 shows changes of the KE axis latitude plotted against DSL differences averaged over $145^{\circ}-$
189 170°E , $35^{\circ}-40^{\circ}\text{N}$ which contains the KE axis latitudes during the analysis period. The DSL differences
190 are significantly correlated with the northward migration of the KE latitude. The relationship becomes
191 stronger as the greenhouse-gas emissions accumulate (and thus radiative forcing increases) across
192 different scenarios and periods. This is a new finding obtained by the analysis of multiple scenarios until
193 2300.

194 The association between DSL changes and velocity changes at depth is a topic of interest for
195 this study. Figure 8 shows that the eastward flow increase (decrease) in the northern (southern) side of the
196 KE, independently of scenario and period, is consistent with the northward KE migration. Another
197 interesting feature is that the velocity changes contains signature of shallowing, which is more clearly
198 seen in the vertical profile of the horizontally averaged zonal geostrophic velocity (Fig. 9a). This is

199 associated with velocity weakening in deeper levels, probably because of enhanced upper ocean
200 stratification due to surface warming and freshening (Fig. 9b).

201

202 4. Atmospheric Forcing

203 In this section, we analyze heat flux and wind stress to show how external forcings of the ocean
204 cause changes in DSL. We focus particular attention on how these forcings influence density reduction of
205 the STMW and northward migration of the KE, which were documented in the previous section.

206 First, we examine the downward net heat flux (positive when ocean gains heat), which may be
207 related to density change of the STMW (Suzuki and Ishii 2011a; Luo et al. 2009). We first calculate the
208 heat flux anomaly in each year by subtracting its mean value of last 30 years in 20th century, and then
209 integrate it from 1971 to 2100 (Figs. 10a and 10b). The integrated downward heat flux anomaly is large in
210 high latitudes (north of 50°N) and to the south and southeast of Japan. The former causes a large
211 temperature increase in higher latitudes, but this heat uptake contributes less to local density, and thus to
212 DSL, than in lower latitudes because of the nonlinearity of the density equation for sea water. The
213 mid-latitude positive integrated heat flux anomalies are located to the south of the climatological mean
214 negative maximum (i.e., the location of maximum heat loss from the ocean over KE), and negative
215 anomalies occur to the north of the climatological mean negative maximum. This spatial pattern
216 represents northward migration of the heat flux field. It implies a link between the heat flux anomaly and

217 northward migration of the KE. Area-averaged downward net heat flux continually increases south and
218 southeast of Japan until the middle of the 23rd (21st) century for the RCP8.5 (RCP4.5) scenario (Fig.
219 10c).

220 The relation between changes in downward net heat flux and local density of the STMW is
221 confirmed by analysis of differences among models (Fig. 11). Here, we limit our analysis of epochal
222 differences, considering only between the ends of the 20th and 21st centuries because we have only four
223 models for which heat flux data are available until 2300, and this is too few for analysis of the
224 relationship among models. Local density change in the STMW is negatively correlated with integrated
225 downward heat flux anomalies south of Japan. Further investigation revealed that reduced atmospheric
226 cooling in winter contributes more to STMW density decrease than increased atmospheric heating in
227 summer (not shown). This means that anomalous ocean heat uptake in winter results in lighter water mass
228 in the STMW. As shown in the previous section, the lower density of this water mass is important in
229 producing the maximal sea-level rise to the east of Japan.

230 The aforementioned possible link between the time-integrated downward heat flux anomaly to
231 the south of Japan and northward KE migration is examined with various climate models (Fig. 12). The
232 changes in downward net heat flux are strongly related to meridional migration of the KE axis latitude,
233 with a correlation coefficient of 0.84 (0.95) for RCP8.5 (RCP4.5). This indicates that the northward KE
234 migration is closely related to the anomalous heat flux south of Japan. Since downward heat flux takes its

235 minimum along the KE axis (see contours of Figs. 10a and 10b), downward net heat flux will be
236 increased (reduced) in the south (north) of its axis when it moves northward. Therefore, KE migration,
237 integrated heat flux anomalies, and density changes of STMW are related. A possible causality is that the
238 KE northward migration accounts for producing lighter water for the STMW through the anomalous
239 ocean heat uptake south of the KE axis until 2100. This chain of causality, however, is not dominant
240 factor for STMW density change, because the correlation between the STMW density change and
241 integrated heat flux anomaly is moderate ($r=-0.45$ in Fig. 11a) and because the density decrease of STMW
242 rather than the northward KE migration plays a more important role in DSL changes in the 21st century as
243 mentioned above.

244 The meridional migration of the KE can be caused by variations of wind distribution because
245 the KE participates in wind-driven circulation over the North Pacific. Figures 13a and 13b show the
246 differences in zonal wind stress between the 1971–2000 and 2071–2100 periods under RCP8.5 and
247 RCP4.5, respectively. Zonal wind stress is enhanced (weakened) to the north (south) of the climatological
248 maximum zonal wind, centered around 40°N across the North Pacific, with stronger magnitudes for
249 RCP8.5 than for RCP4.5. This spatial pattern indicates northward migration of the zonal wind stress field,
250 consistent with previous studies (Sueyoshi and Yasuda 2012; Zhang et al. 2014). The wind stress curl
251 field also exhibits northward migration of time-mean pattern, and its change is characterized by an
252 anticyclonic anomalies extending eastward from the east coast of Japan (not shown). The latitude of

253 zonally averaged zonal wind stress maximum moves 1 (0.4) degrees to the north by 2100 in RCP8.5
254 (RCP4.5). Anomaly time series of the latitude of zero Sverdrup stream function (SSF) at 150° E over the
255 North Pacific (150°E–160°W) exhibit northward movement until roughly the middle of the 21st (23rd)
256 century for RCP4.5 (RCP8.5) (Fig. 13c), though internal variability in each model is not averaged out
257 especially in 6-model MME.

258 Northward migration of the KE is significantly correlated (at the 5% significance) with that of
259 the latitude of zero SSF under RCP8.5 ($r=0.54$, $p<0.01$), but the correlation under RCP4.5 is not
260 significant ($r=0.21$, $p=0.27$) (Fig. 14). This means that although the MME indicates that both the KE axis
261 and zero SSF latitude move northward, different KE migrations among models are not well explained by
262 the shift in zero SSF latitude under RCP4.5. The stronger relationship in RCP8.5 relative to RCP4.5
263 suggests that the uncertainty in RCP4.5 may arise from internal variability of the ocean, though further
264 studies are necessary to clarify this. It is interesting to note that the regression slopes are all shallower
265 than unity, meaning that the northward migration of the KE is smaller than migration of the zero SSF
266 latitude in many models. This migration discrepancy may be due to a strong non-linearity of the KE,
267 although its specific contribution is uncertain.

268 The northward migration of the SSF field and hence that of the zonal wind stress is likely
269 influenced by the change of large-scale atmospheric circulation. Figure 15 shows the MME changes of
270 sea-level pressure (SLP) over the North Pacific. Between the ends of the 20th and 21st centuries, SLP

271 changes are characterized by decreases in the Bering Sea and increases in the central and western North
272 Pacific between 30°N and 40°N (Figs. 15a and 15c). This pattern of change in SLP indicates overall
273 deepening and northward shifting of the Aleutian Low, consistent with previous studies (e.g., Sueyoshi
274 and Yasuda 2012; Oshima et al. 2012; Collins et al. 2013; Gan et al. 2017). These changes to the Aleutian
275 Low continue after 2100 and are accompanied by weakening of the subtropical high (Fig. 15b). The
276 spatial patterns of changes in SLP are associated with positive trends of the annular modes as well as with
277 poleward expansion of the Hadley circulation (Miller et al. 2006; Rauthe et al. 2004; Collins et al. 2013).
278 These two phenomena may result from global warming (Cheon et al. 2012; Frierson et al. 2007; Hu et al.
279 2013; Johanson and Fu 2009; Lu et al. 2007; Previdi and Liepert 2007)..

280

281 5. Discussion and Summary

282 We investigated change in DSL over the North Pacific until 2300 under middle and high
283 greenhouse-gas emission scenarios (RCP4.5 and RCP8.5, respectively) by analyzing MME along with
284 differences among models, including subsurface density and velocity fields, using output from CMIP5
285 models. This is the first study of subsurface density and velocity fields for the future DSL change in the
286 western North Pacific. Hence, our analysis has provided more comprehensive understanding of future
287 DSL changes.

288 The DSL changes in the North Pacific are characterized by DSL rise in the western North

289 Pacific around the KE (Fig. 1), as reported in previous studies (Yin et al. 2010; Yin 2012; Sueyoshi and
290 Yasuda 2012; Zhang et al. 2014; Church et al. 2013; Slangen et al. 2014). Around the KE, DSL continues
291 to rise roughly through the 21st century under RCP4.5 and until the end of the 23rd century under RCP8.5,
292 indicating that DSL will continue to change for decades after stabilization of radiative forcing (Fig. 2).
293 The localized DSL change around the KE is related to a density decrease of the STMW and to northward
294 migration of the KE (Fig. 3). Both of them induce DSL rise in the western North Pacific by 2100 and
295 2300. Specifically, the density decreases more strongly in the region of STMW than that around the KE
296 axis until 2100 under both RCP4.5 and RCP8.5, whereas the density decreases more strongly around the
297 KE axis than in the STMW region after 2100 under RCP8.5 (Fig. 4). The different patterns of
298 density changes between the two periods result in the different spatial distributions of DSL
299 changes by 2100 and 2300. The local density decrease in the STMW and the KE northward migration
300 also explain different DSL changes among models (Figs. 6 and 7). The KE migration is confirmed by
301 subsurface geostrophic velocity analysis (Fig. 8). The KE exhibits not only a simple meridional migration
302 but also a stronger concentration near the surface, probably due to enhanced stratification (Fig. 9).

303 The reduction in STMW density is likely to be caused at least in part by high heat uptake to the
304 south and southeast of Japan, where the Kuroshio and its extension flow (Figs. 10 and 12). The excess
305 heat flux in this region is very strongly related to the northward migration of the KE (Fig. 12). This
306 northward KE shift is forced, at least in part, by changes in wind distribution, and the northward shift of

307 the latitude of zero SSF results in northward shift of the KE (Figs. 13 and 14). The poleward shift of the
308 wind field is related to the poleward shift of the atmospheric circulation (Fig. 15), which is probably
309 related to the poleward expansion of the Hadley circulation. The major features and mechanisms of DSL
310 rise in the western North Pacific between 2000 and 2100 are summarized in Fig. 16.

311 As discussed in Section 1, previous studies suggest that the strong DSL rise in the western
312 North Pacific around the KE is due to anomalous heat uptake, mainly due to STMW (Lowe and Gregory
313 2006; Suzuki and Ishii 2011b), the northward migration of the KE (Sueyoshi and Yasuda 2012; Zhang et
314 al. 2014) or KE intensification (Sueyoshi and Yasuda 2012). Among these three mechanisms, the first and
315 last, anomalous heat uptake by the STMW and KE intensification may be closely associated. This is
316 because the KE strength, defined by Sueyoshi and Yasuda (2012) as the meridional DSL difference
317 between 34°N and 42°N for a 150° – 165°E range, is the most likely to be dominated by a change in DSL
318 at 34°N , which is within the meridional range of the STMW (Fig. 4). DSL change is much stronger at
319 34°N than at 42°N (Fig. 1), even using the composite difference for models that exhibit strong KE
320 intensification (see Fig. 9 of Sueyoshi and Yasuda 2012). Consequently, we suggest that KE
321 intensification may be better understood as an aspect of the heat uptake of STMW. This means that heat
322 uptake by the STMW and meridional migration of the KE are the two essential mechanisms for DSL
323 changes around the KE, though these two mechanisms are not totally independent, as shown by a
324 significant correlation between the KE meridional migration and excess heat uptake to the south and

325 southeast of Japan (Fig. 12).

326 The DSL changes attributable to these two mechanisms differ substantially among models.
327 Figure 17 shows the local density difference for each model in the western North Pacific (145°–170°E)
328 under RCP8.5. Most of the models exhibit local density differences for the STMW, but the magnitudes of
329 the differences have wide variability, consistent with the situation in Fig. 5. Furthermore, many models
330 (specifically, CMCC-CESM, CMC-CM, CMCC-CM5, FGOALS-g2, and IPSL-CM5A-MR) exhibit
331 stronger changes associated with the KE, and some other models (CanESM2, hadGEM2-CC,
332 HadGem2-ES, MIROC-ESM, MIROC-ESM-CHEM, MPI-ESM-MR) exhibit two maxima,
333 corresponding to the STMW and the KE.

334 The inter-model differences of future response are bringing into question how these large
335 inter-model differences are related to the mean state differences. To address this question,
336 we apply the inter-model singular value decomposition (SVD) analysis that was used by Lyu
337 et al. (2016) to examine the relationship between climatological mean state and interdecadal
338 variability patterns among CMIP5 models. We first derive the departures of each model's
339 DSL averaged for 1971-2000 period and the DSL difference between 1971-2000 and
340 2071-2100 periods from the MME mean patterns in the North Pacific (120°E-115°W,
341 20°N-60°N), and then apply the inter-model SVD analysis. The first mode explains only 12%
342 of total variance, and there is no significant co-variation in the western North Pacific where

343 we focus on in this study. Therefore, the inter-model differences in the DSL rise around the KE is not
344 well explained by the mean state difference. Future work is required for the better understanding of the
345 reasons for model differences that would lead to better overall understanding and more certain
346 projections.

347

348 Acknowledgements

349 We thank Dr. Tatsuo Suzuki, Dr. Tamaki Yasuda, and Dr. Yoshi N. Sasaki for fruitful
350 discussions. We also thank Dr. Tamaki Yasuda for providing some of the CMIP5 data used in this study.

351 We acknowledge the climate modeling groups and the World Climate Research Programme's Working
352 Group on Coupled Modelling for producing and making their model output available, and the U.S.
353 Department of Energy and other agencies contributing Earth System Grid Federation for their roles in
354 collecting and archiving the model output. This work was supported by the Japan Society for the
355 Promotion of Science (JSPS) KAKENHI Grant Numbers 26287110, 26610146, and 15H01606.

356

357 References

- 358 Cheon, W. G., Y.-G. Park, S.-W. Yeh, and B.-M. Kim (2012) Atmospheric impact on the northwestern
359 Pacific under a global warming scenario. *Geophys Res Lett* 39: L16709. doi:
360 10.1029/2012GL052364
- 361 Church, J.A., P.U. Clark, A. Cazenave, J.M. Gregory, S. Jevrejeva, A. Levermann, M.A. Merrifield, G.A.
362 Milne, R.S. Nerem, P.D. Nunn, A.J. Payne, W.T. Pfeffer, D. Stammer and A.S. Unnikrishnan
363 (2013) Sea Level Change. In: *Climate Change 2013: The Physical Science Basis. Contribution*
364 *of Working Group I to the Fifth Assessment Report of the Intergovernmental Panel on Climate*
365 *Change* [Stocker, T.F., D. Qin, G.-K. Plattner, M. Tignor, S.K. Allen, J. Boschung, A. Nauels, Y.
366 Xia, V. Bex and P.M. Midgley (eds.)]. Cambridge University Press, Cambridge, United
367 Kingdom and New York, NY, USA.
- 368 Collins, M., R. Knutti, J. Arblaster, J.-L. Dufresne, T. Fichet, P. Friedlingstein, X. Gao, W.J. Gutowski,
369 T. Johns, G. Krinner, M. Shongwe, C. Tebaldi, A.J. Weaver and M. Wehner (2013) Long-term
370 Climate Change: Projections, Commitments and Irreversibility. In: *Climate Change 2013: The*
371 *Physical Science Basis. Contribution of Working Group I to the Fifth Assessment Report of the*
372 *Intergovernmental Panel on Climate Change* [Stocker, T.F., D. Qin, G.-K. Plattner, M. Tignor,
373 S.K. Allen, J. Boschung, A. Nauels, Y. Xia, V. Bex and P.M. Midgley (eds.)]. Cambridge
374 University Press, Cambridge, United Kingdom and New York, NY, USA.
- 375 Frierson, D. M. W., J. Lu, and G. Chen (2007) Width of the Hadley cell in simple and comprehensive

- 376 general circulation models. *Geophys Res Lett* 34: L18804. doi:10.1029/2007GL031115
- 377 Gan, B., L. Wu, F. Jia, S. Li, W. Cai, H. Nakamura, M. A. Alexander, and A. J. Miller (2017) On the
378 Response of the Aleutian Low to Greenhouse Warming, *J Clim.* doi:
379 10.1175/JCLI-D-15-0789.1, in press.
- 380 Gregory, J. M., et al. (2001) Comparison of results from several AOGCMs for global and regional
381 sea-level change 1900-2100, *Clim Dyn* 18: 225-240
- 382 Hu, Y., L. Tao, and J. Liu (2013). Poleward expansion of the hadley circulation in CMIP5 simulations.
383 *Adv Atmos Sci* 30: 790-795.
- 384 Ishii, M., and M. Kimoto (2009). Reevaluation of historical ocean heat content variations with
385 time-varying XBT and MBT depth bias corrections. *J Oceanogr* 65: 287-299
- 386 Johanson, C. M., and Q. Fu (2009). Hadley Cell Widening: Model Simulations versus Observations. *J*
387 *Clim* 22: 2713-2725
- 388 Liddicoat, S., C. Jones, and E. Robertson (2013) CO2Emissions Determined by HadGEM2-ES to be
389 Compatible with the Representative Concentration Pathway Scenarios and Their Extensions. *J*
390 *Clim* 26: 4381-4397
- 391 Liu Z.-J., S. Minobe, Y. N. Sasaki and M. Terada (2016) Dynamical downscaling of future sea-level
392 change in the western North Pacific using ROMS. *J. Oceanogr.*, in press, doi:
393 10.1007/s10872-016-0390-0

- 394 Lowe, J. A., and J. M. Gregory (2006) Understanding projections of sea level rise in a Hadley Centre
395 coupled climate model. *J Geophys Res* 111: C11014. doi:10.1029/2005JC003421
- 396 Lu, J., G. A. Vecchi, and T. Reichler (2007) Expansion of the Hadley cell under global warming. *Geophys*
397 *Res Lett* 34: L06805. doi: 10.1029/ 2006GL028443
- 398 Luo, Y. Y., Q. Y. Liu, and L. M. Rothstein (2009) Simulated response of North Pacific Mode Waters to
399 global warming. *Geophys Res Lett* 36: L23609. doi:10.1029/2009GL040906
- 400 Lyu, K., X. Zhang, J. A. Church, and J. Hu (2016), Evaluation of the interdecadal variability of sea
401 surface temperature and sea level in the Pacific in CMIP3 and CMIP5 models, *Int. J. Climatol.*,
402 36, 3723-3740. doi:10.1002/joc.4587
- 403 Miller, R. L., G. A. Schmidt, and D. T. Shindell (2006) Forced annular variations in the 20th century
404 Intergovernmental Panel on Climate Change Fourth Assessment Report models, *J Geophys Res*
405 111: D18101
- 406 Mitrovica, J. X., N. Gomez, E. Morrow, C. Hay, K. Letychev, and M. E. Tamisiea (2011) On the
407 robustness of predictions of sea level fingerprints, *Geophys J Int*, 187, 729-742
- 408 Nicholls, R. J., S. E. Hanson, J. A. Lowe, R. A. Warrick, X. Lu, and A. J. Long (2014) Sea-level scenarios
409 for evaluating coastal impacts. *WIREs Clim Change* 2014, 5: 129-150. doi: 10.1002/wcc.253
- 410 Oshima, K., Y. Tanimoto, and S.-P. Xie (2012) Regional Patterns of Wintertime SLP Change over the
411 North Pacific and Their Uncertainty in CMIP3 Multi-Model Projections. *J Meteorol Soc Jpn*

- 412 90A(0): 385-396. doi:10.2151/jmsj.2012-A23
- 413 Pardaens, A. K., J. M. Gregory, and J. A. Lowe (2010) A model study of factors influencing projected
414 changes in regional sea level over the twenty-first century., *Clim Dyn* 36: 2015-2033
- 415 Peltier, W. R. (2004), GLOBAL GLACIAL ISOSTASY AND THE SURFACE OF THE ICE-AGE
416 EARTH: The ICE-5G (VM2) Model and GRACE, *Annu Rev Earth Planet Sci*, 32, 111-149
- 417 Previdi, M., and B. G. Liepert (2007) Annular modes and Hadley cell expansion under global warming.
418 *Geophys Res Lett* 34: L22701. doi:10.1029/2007GL031243
- 419 Rauthe, M., A. Hense, and H. Paeth (2004) A model intercomparison study of climate change-signals in
420 extratropical circulation. *Int J Clim* 24: 643-662
- 421 Slangen, A. B. A., M. Carson, C. A. Katsman, R. S. W. van de Wal, A. Köhl, L. L. A. Vermeersen, and D.
422 Stammer (2014) Projecting twenty-first century regional sea-level changes. *Climatic Change*
423 124: 317-332. doi:10.1007/s10584-014-1080-9
- 424 Sueyoshi, M., and T. Yasuda (2012) Inter-model variability of projected sea level changes in the western
425 North Pacific in CMIP3 coupled climate models. *J Oceanogr* 68: 533-543
- 426 Sugimoto, S., K. Hanawa, T. Watanabe, T. Suga, and S.-P. Xie (2017) Enhanced warming of the
427 subtropical mode water in the North Pacific and North Atlantic. *Nat Clim Change* (online). doi:
428 doi:10.1038/nclimate3371
- 429 Suzuki, T., and M. Ishii (2011a) Regional distribution of sea level changes resulting from enhanced

- 430 greenhouse warming in the Model for Interdisciplinary Research on Climate version 3.2.
431 Geophys Res Lett 38: L02601. doi:10.1029/2010GL045693
- 432 Suzuki, T., and M. Ishii (2011b) Long-term regional sea level changes due to variations in water mass
433 density during the period 1981-2007. Geophys Res Lett 38: L21604.
434 doi:10.1029/2011GL049326
- 435 Taylor, K. E., R. J. Stouffer, and G. A. Meehl (2012) An Overview of CMIP5 and the Experiment Design.
436 Bull Amer Meteor Soc 93: 485-498. doi: 10.1175/BAMS-D-11-00094.1
- 437 Thomson, A.M., Calvin, K.V., Smith, S.J. et al. (2011) RCP4.5: a pathway for stabilization of radiative
438 forcing by 2100. Climatic Change 109: 77. doi:10.1007/s10584-011-0151-4
- 439 Timmermann, A., S. McGregor, and F.-F. Jin (2010) Wind Effects on Past and Future Regional Sea Level
440 Trends in the Southern Indo-Pacific. J Clim 23: 4429-4437
- 441 Wada, Y., L. P. H. van Beek, F. C. Sperna Weiland, B. F. Chao, Y.-H. Wu, and M. F. P. Bierkens (2012),
442 Past and future contribution of global groundwater depletion to sea-level rise, Geophys Res
443 Lett 39: L09402. doi:10.1029/2012GL051230
- 444 Willis, J. K., and J. A. Church (2012) Climate change. Regional sea-level projection. Science, 336:
445 550-551
- 446 Yin, J. (2012) Century to multi-century sea level rise projections from CMIP5 models. Geophys Res Lett
447 39: L17709. doi:10.1029/2012GL052947

- 448 Yin, J., S. M. Griffies, and R. J. Stouffer (2010) Spatial Variability of Sea Level Rise in Twenty-First
449 Century Projections J Climate 23: 4585-4607
- 450 Zhang, X., J. A. Church, S. M. Platten, and D. Monselesan (2014) Projection of subtropical gyre
451 circulation and associated sea level changes in the Pacific based on CMIP3 climate models.
452 Clim Dyn 43: 131-144
- 453
- 454

455 Table

456 Table 1. CMIP5 models used in this study. HF indicates that downward net heat flux data (*hfds* in CMIP5)

457 were available to the authors.

	Model	Country	2100 RCP8.5 (34 models)	2100 RCP4.5 (32 models)	2300 RCP8.5 (6 models)	2300 RCP4.5 (6 models)
A	BCC-CSM1-1	China	✓ (HF)	✓	✓ (HF)	✓
B	CNRM-CM5	France	✓ (HF)	✓	✓ (HF)	✓
C	GISS-E2-R	USA	✓ (HF)	✓	✓ (HF)	✓
D	HadGEM2-ES	UK	✓	✓	✓	✓
E	IPSL-CM5A-LR	France	✓	✓	✓	✓
F	MPI-ESM-LR	Germany	✓ (HF)	✓ (HF)	✓ (HF)	✓ (HF)
G	ACCESS1-0	Australia	✓ (HF)	✓		
H	ACCESS1-3	Australia	✓ (HF)	✓		
I	BCC-CSM1-1-M	China	✓ (HF)	✓ (HF)		
J	CCSM4	USA	✓	✓		
K	CESM1-BGC	USA	✓	✓		
L	CESM1-WACCM	USA	✓	✓		
M	CMCC-CESM	Italy	✓ (HF)			
N	CMCC-CM	Italy	✓ (HF)	✓ (HF)		
O	CMCC-CMS	Italy	✓ (HF)	✓ (HF)		
P	CSIRO-Mk3-6-0	Australia	✓ (HF)	✓		
Q	CanESM2	Canada	✓	✓		
R	FGOALS-g2	China	✓ (HF)	✓ (HF)		
S	FGOALS-s2	China	✓ (HF)	✓		
T	FIO-ESM	China	✓ (HF)	✓		
U	GFDL-CM3	USA	✓	✓		
V	GFDL-ESM2G	USA	✓ (HF)	✓		
W	GFDL-ESM2M	USA	✓	✓		
X	HadGEM2-CC	UK	✓	✓		
Y	IPSL-CM5A-MR	France	✓	✓		
Z	IPSL-CM5B-LR	France	✓	✓		
a	MIROC-ESM	Japan	✓ (HF)	✓ (HF)		
b	MIROC-ESM-CHEM	Japan	✓ (HF)	✓ (HF)		
c	MIROC5	Japan	✓ (HF)	✓		
d	MPI-ESM-MR	Germany	✓ (HF)	✓ (HF)		
e	MRI-CGCM3	Japan	✓ (HF)	✓ (HF)		
f	MRI-ESM1	Japan	✓ (HF)			
g	NorESM1-M	Norway	✓ (HF)	✓		
h	NorESM1-ME	Norway	✓ (HF)	✓		

458

459 Figure captions

460 Figure 1. DSL differences (color) (a) between 1971–2000 and 2071–2100 periods for 34-model MME
461 under RCP8.5, (b) between 1971–2000 and 2071–2100 periods for 32-model MME under RCP4.5, (c)
462 between 2071–2100 and 2271–2300 periods for 6-model MME under RCP8.5, and (d) between 2071–
463 2100 and 2271–2300 periods for 6-model MME under RCP4.5. Panel (e) and (f) is same as (a) and (b) but
464 for 6-model MME. Contours indicate the mean DSL for the periods of (a, b, d, f) 1971–2000 and (c, d)
465 2071–2100. Solid (dashed) blue arrows indicate the KE axis latitude for the periods of (a, b, e, f) 1971–
466 2000 (2071–2100) and (c, d) 2071–2100 (2271–2300). The KE axis latitude is estimated as the center of
467 gravity of eastward geostrophic surface velocity, zonally averaged over 145°–170°E, 25°–50°N.

468

469 Figure 2. Time series of the area-averaged (145°–170°E, 30°–45°N) DSL anomaly from 1971–2000 mean
470 smoothed by applying an 11-year running mean for 34-model MME under RCP8.5 (red), 32-model MME
471 under RCP4.5 (blue), 6-model MME under RCP8.5 (black), and 6-model MME under RCP4.5 (green).

472

473 Figure 3. Same as Figs. 1a–c, but for local steric sea-level differences.

474

475 Figure 4. Zonally averaged (145°–170°E) local density differences (color) (a) between 1971–2000 and
476 2071–2100 periods for 34-model MME under RCP8.5, (b) between 2071–2100 and 2271–2300 periods

477 for 6-model MME under RCP8.5, and (c) between 1971–2000 and 2071–2100 periods for 32-model
478 MME under RCP4.5. Local density is defined as the deviation from global mean density at each level (see
479 text). Contours indicate the mean σ for the periods (a,c) 1971–2000 and (b) 2071–2100.

480

481 Figure 5. Time series of (a) local density anomaly averaged in the STMW region (145° – 170° E, 25° – 35° N,
482 and depth 50–300 m) and (b) the KE-axis latitude anomaly smoothed by applying an 11-year running
483 mean for 34-model MME under RCP8.5 (red), 32-model MME under RCP4.5 (blue), and 6-model MME
484 under RCP8.5 (black).

485

486 Figure 6. Scatter diagram of epoch differences in DSL due to local density averaged in the STMW region
487 (145° – 170° E, 25° – 35° N, and depth 50–300 m) and DSL over the same domain among climate models.

488 The epochs and scenarios are (a) 1971–2000 and 2071–2100 periods under RCP8.5, (b) 2071–2100 and
489 2271–2300 periods under RCP8.5, and (c) 1971–2000 and 2071–2100 periods under RCP4.5. The plus
490 symbol (+) and alphabetical letters denote the MME and the models (Table 1), respectively. Correlation
491 coefficients and p -values are shown in the panels. Solid lines indicate regression lines, while dotted lines
492 denote the lines of slope 1.

493

494 Figure 7. As in Fig. 6, but for epoch differences of KE axis latitude and DSL around the KE axis (145° –

495 170°E, 35°–40°N) among climate models. The dashed line in (c) is the regression line from (a).

496

497 Figure 8. Eastward geostrophic current-speed differences, calculated using the zonally averaged (145°–

498 170°E) in-situ density and sea level (color) (a) between 1971–2000 and 2071–2100 periods for 34-model

499 MME under RCP8.5, (b) between 2071–2100 and 2271–2300 periods for 6-model MME under RCP8.5,

500 and (c) between 1971–2000 and 2071–2100 periods for 34-model MME under RCP4.5. Black, blue, and

501 red contours indicate the mean zonal geostrophic current speed for the periods 1971–2000, 2071–2100,

502 and 2271–2300, respectively.

503

504 Figure 9. Vertical profiles of (a) zonal velocity and (b) σ averaged in 145°–170°E, 27°N–47°N for (black

505 dashed curve) 1971–2000 period in the historical experiment, (red curve) 2071–2000 period under

506 RCP8.5, (blue curve) 2071–2000 period under RCP4.5, and (black solid curve) 2272–2300 period under

507 RCP8.5.

508

509 Figure 10. Time-integrated downward net heat flux anomaly (color) for (a) 23-model MME under

510 RCP8.5 and (b) 9-model MME under RCP4.5. Panel (c) shows the time series of area-averaged

511 downward net heat flux (130°–160°E, 25°–35°N) anomaly from 1971–2000 mean smoothed by applying

512 an 11-year running mean for the following: (red) 23-model MME under RCP8.5, (blue) 9-model MME

513 under RCP4.5, and (black) 4-model MME under RCP8.5. Contours in panels (a) and (b) indicate the
514 mean downward net heat flux for the period 1971–2000. The domain for area averaging is marked by the
515 box in (a).

516 Figure 11. Scatter diagram of epoch differences of the local density averaged in the STMW region (145°–
517 170°E, 25°–35°N, and depth 50–300 m) and integrated downward net heat flux averaged south of the KE
518 (130°–160°E, 25°–35°N) among climate models between 1971–2000 and 2071–2100 periods. The
519 scenarios are (a) RCP8.5 and (c) RCP4.5. The plus symbols (+) and alphabetical letters denote MME and
520 the models (Table 1), respectively. Correlation coefficients and *p*-values are shown. Solid lines indicate
521 the regression line from the data points. The dashed line in (b) is the regression line from (a).

522

523 Figure 12. As in Fig. 11, but for epoch differences of the KE-axis latitude and integrated downward net
524 heat flux averaged south of the KE (135°–145°E, 30°–35°N) among climate models. The dashed line in
525 (b) is the regression line from (a).

526

527 Figure 13. Zonal wind stress differences between 1971–2000 and 2071–2100 periods (color) (a) for
528 34-model MME under RCP8.5 and (b) for 32-model MME under RCP4.5. Contours indicate the mean
529 zonal wind stress for the period 1971–2000. (c) Anomaly time series of the latitude of zero SSF at 150°E
530 relative to 1971–2000 mean smoothed by applying an 11-year running mean for the following: (red)

531 34-model MME under RCP8.5, (blue) 32-model MME under RCP4.5, and (black) 6-model MME under
532 RCP8.5. The SSF is calculated by zonally integrating wind stress curl westward from the eastern
533 boundary (i.e., Sverdrup Balance).

534

535 Figure 14. As in Fig. 6, but for epoch differences of the KE-axis latitude and the latitude of zero SSF at
536 150°E among climate models. Dotted lines indicate slope 1.

537

538 Figure 15. Epoch differences of SLP (color) (a) between 1971–2000 and 2071–2100 periods for 34-model
539 MME under RCP8.5, (b) between 2071–2100 and 2271–2300 periods for 6-model MME under RCP8.5,
540 and (c) between 1971–2000 and 2071–2100 periods for 32-model MME under RCP4.5. Contours indicate
541 the mean SLP for the periods (a, c) 1971–2000 and (b) 2071–2100.

542

543 Figure 16. Schematic diagram illustrating the mechanism of DSL rise in the western North Pacific. DSL
544 rises around the KE is associated with the density decrease of the STMW and northward KE migration.
545 The STMW density decrease is caused by anomalous downward net heat flux to the south and southeast
546 of Japan, while the northward KE migration is due to the poleward shift of the wind stress field. The
547 excess heat flux is also strongly related to the northward migration of the KE. The solid arrows indicate
548 the inter-model relationships that are significant at 5% significance level for both the RCP4.5 and 8.5,

549 while dashed arrows indicate the relationships that are significant only for RCP8.5 but not for RCP4.5.

550

551 Figure 17. Zonally averaged (145°–170°E) local density differences between 1971–2000 and 2071–2100

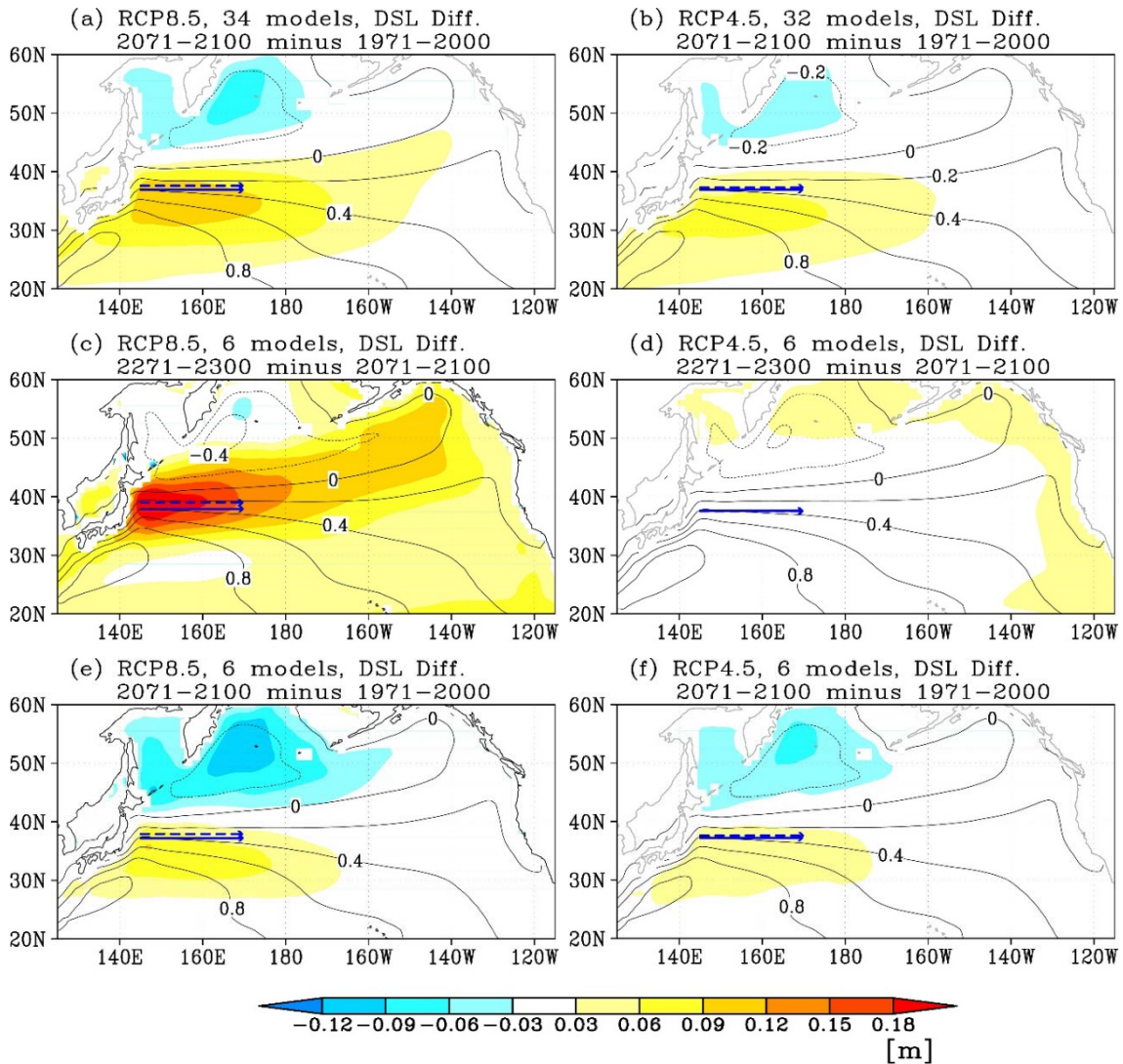
552 periods under RCP8.5 for each model (color). Contours indicate the mean σ for the period 1971–2000.

553 MME indicates the MME mean.

554

555 Figures

556



557

558 Figure 1. DSL differences (color) (a) between 1971–2000 and 2071–2100 periods for 34-model MME

559 under RCP8.5, (b) between 1971–2000 and 2071–2100 periods for 32-model MME under RCP4.5, (c)

560 between 2071–2100 and 2271–2300 periods for 6-model MME under RCP8.5, and (d) between 2071–

561 2100 and 2271–2300 periods for 6-model MME under RCP4.5. Panel (e) and (f) is same as (a) and (b) but

562 for 6-model MME. Contours indicate the mean DSL for the periods of (a, b, d, f) 1971–2000 and (c, d)

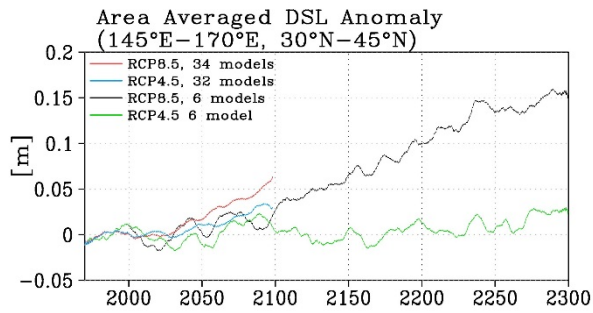
563 2071–2100. Solid (dashed) blue arrows indicate the KE axis latitude for the periods of (a, b, e, f) 1971–

564 2000 (2071–2100) and (c, d) 2071–2100 (2271–2300). The KE axis latitude is estimated as the center of

565 gravity of eastward geostrophic surface velocity, zonally averaged over 145°–170°E, 25°–50°N.

566

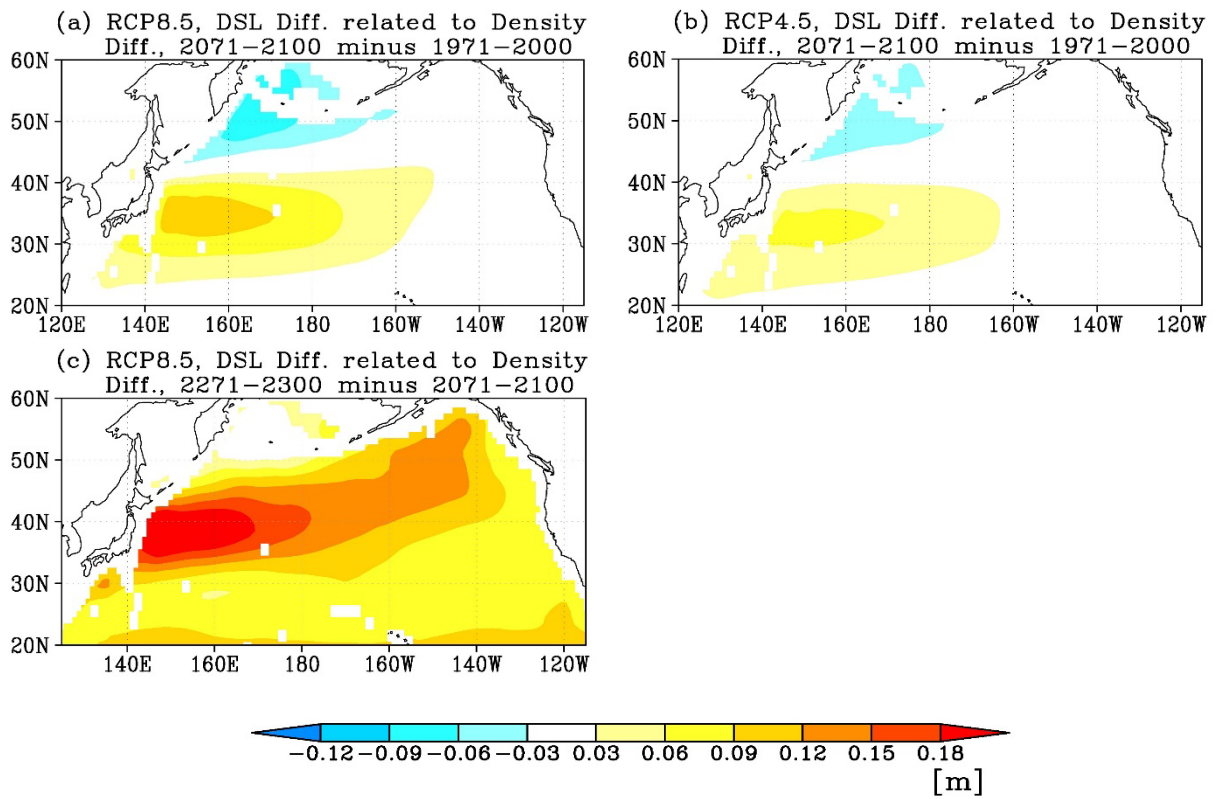
567



568

569 Figure 2. Time series of the area-averaged (145°–170°E, 30°–45°N) DSL anomaly from 1971–2000 mean
570 smoothed by applying an 11-year running mean for 34-model MME under RCP8.5 (red), 32-model MME
571 under RCP4.5 (blue), 6-model MME under RCP8.5 (black), and 6-model MME under RCP4.5 (green).

572

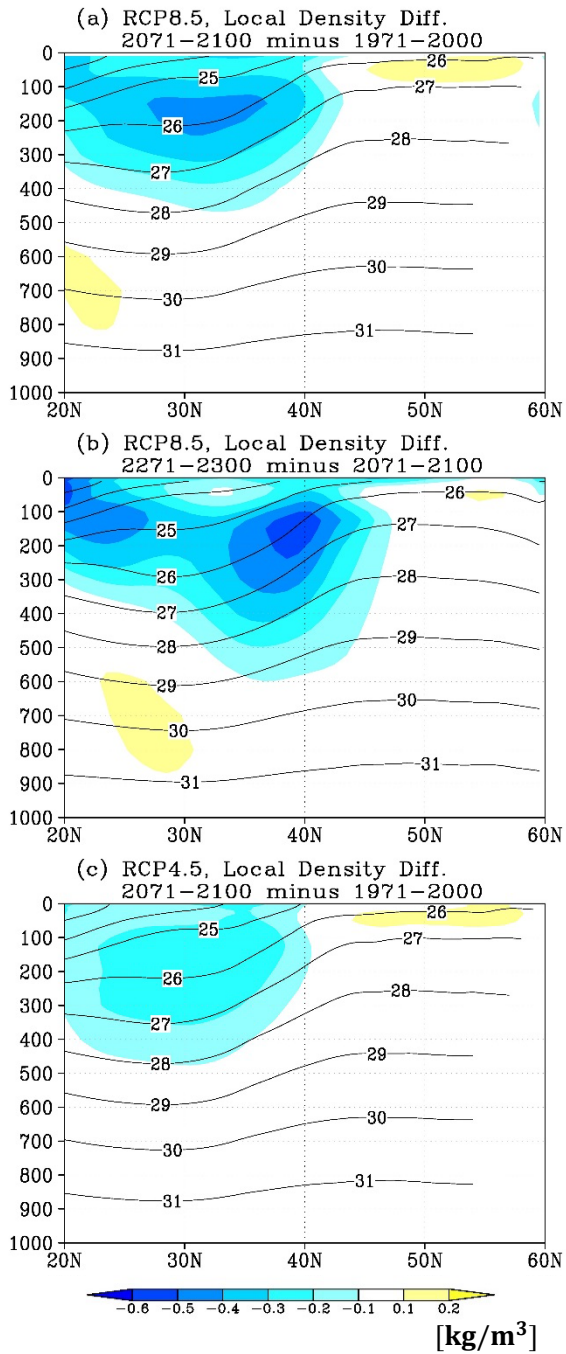


573

574 Figure 3. Same as Figs. 1a–c, but for local steric sea-level differences.

575

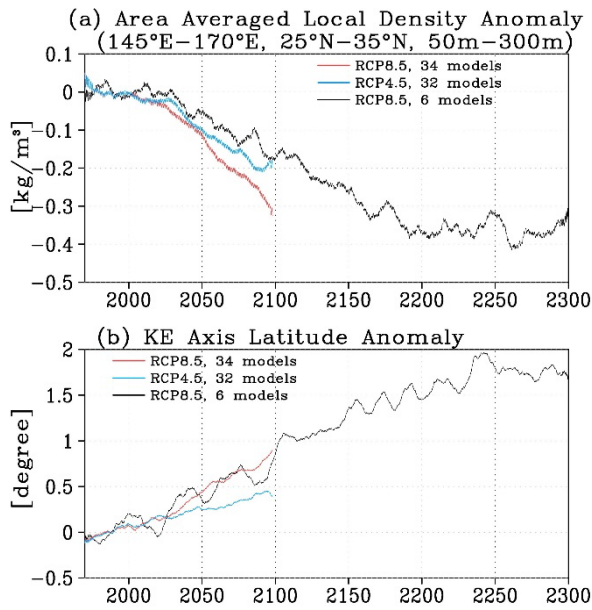
576



577

578 Figure 4. Zonally averaged (145° – 170° E) local density differences (color) (a) between 1971–2000 and
 579 2071–2100 periods for 34-model MME under RCP8.5, (b) between 2071–2100 and 2271–2300 periods
 580 for 6-model MME under RCP8.5, and (c) between 1971–2000 and 2071–2100 periods for 32-model
 581 MME under RCP4.5. Local density is defined as the deviation from global mean density at each level (see
 582 text). Contours indicate the mean σ for the periods (a,c) 1971–2000 and (b) 2071–2100.

583



584

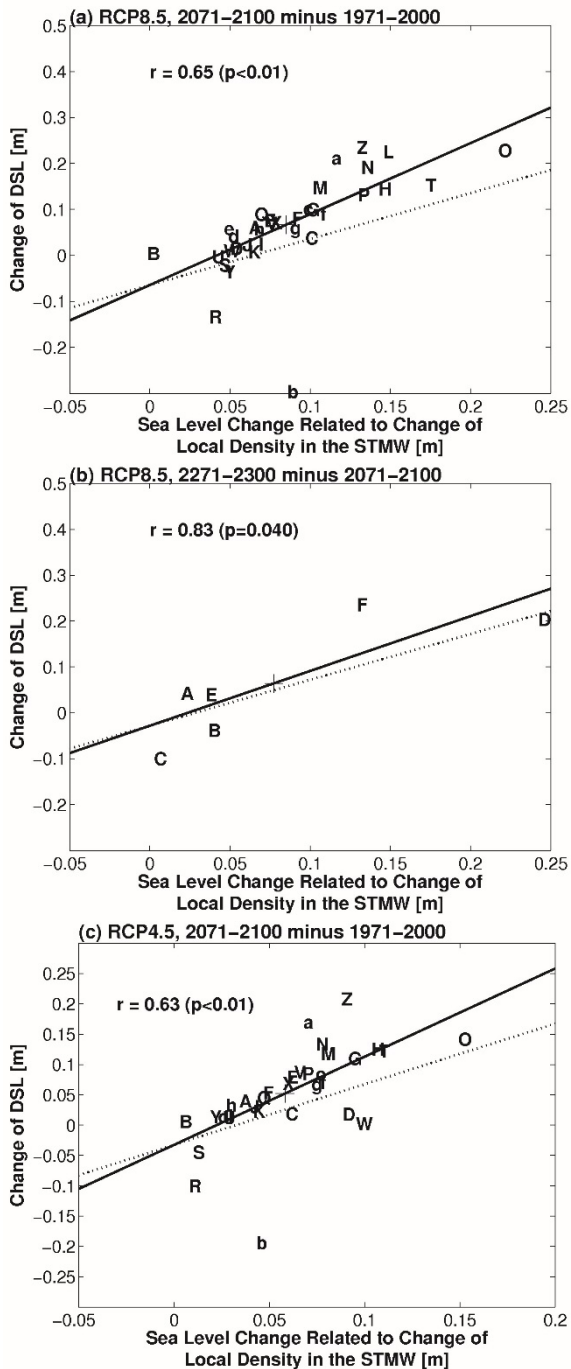
585 Figure 5. Time series of (a) local density anomaly averaged in the STMW region (145°–170°E, 25°–35°N,

586 and depth 50–300 m) and (b) the KE-axis latitude anomaly smoothed by applying an 11-year running

587 mean for 34-model MME under RCP8.5 (red), 32-model MME under RCP4.5 (blue), and 6-model MME

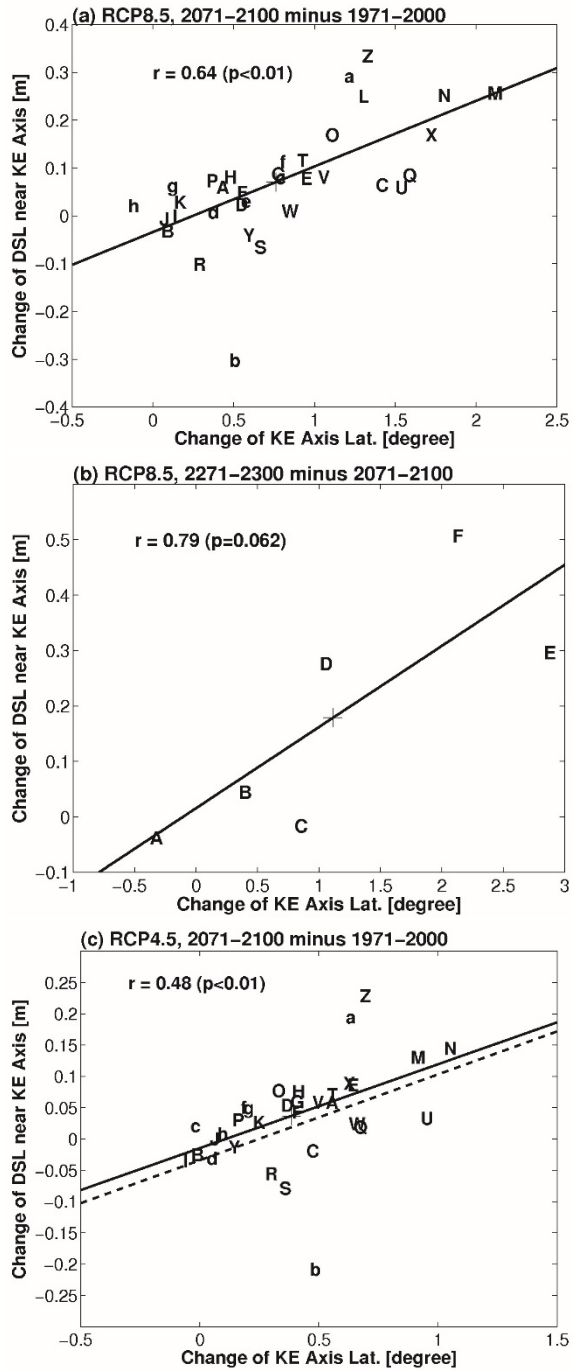
588 under RCP8.5 (black).

589



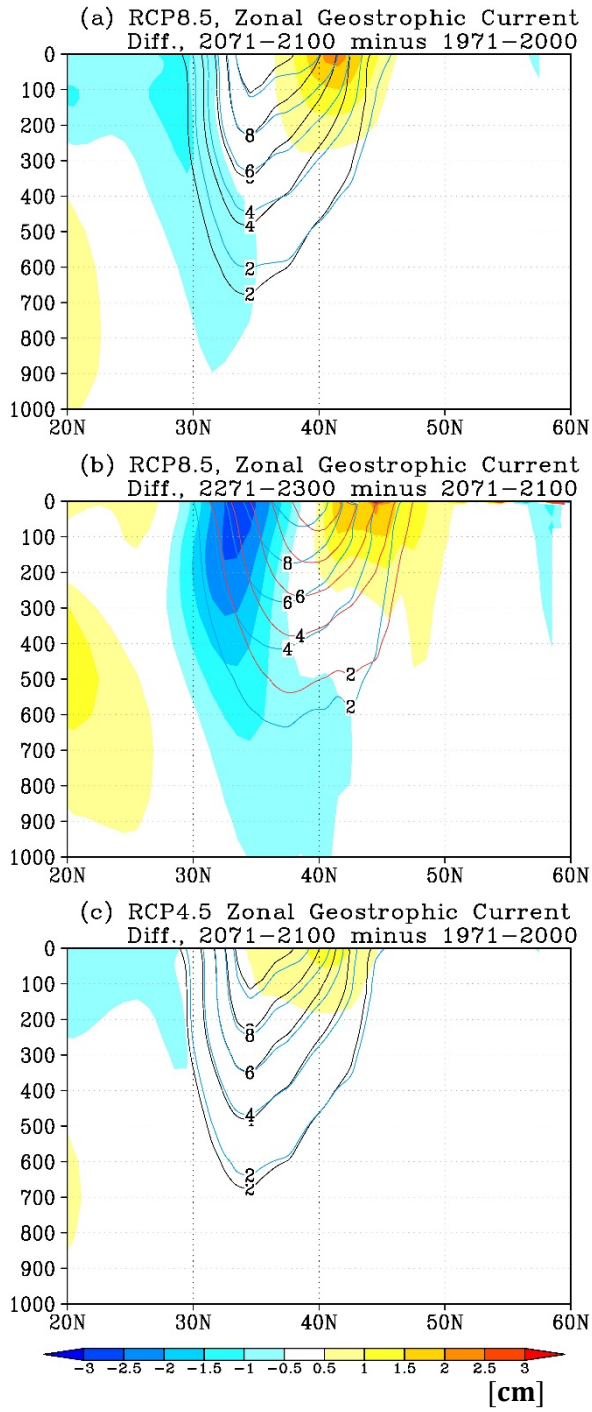
590

591 Figure 6. Scatter diagram of epoch differences in DSL due to local density averaged in the STMW region
 592 (145° – 170° E, 25° – 35° N, and depth 50–300 m) and DSL over the same domain among climate models.
 593 The epochs and scenarios are (a) 1971–2000 and 2071–2100 periods under RCP8.5, (b) 2071–2100 and
 594 2271–2300 periods under RCP8.5, and (c) 1971–2000 and 2071–2100 periods under RCP4.5. The plus
 595 symbol (+) and alphabetical letters denote the MME and the models (Table 1), respectively. Correlation
 596 coefficients and p -values are shown in the panels. Solid lines indicate regression lines, while dotted lines
 597 denote the lines of slope 1.



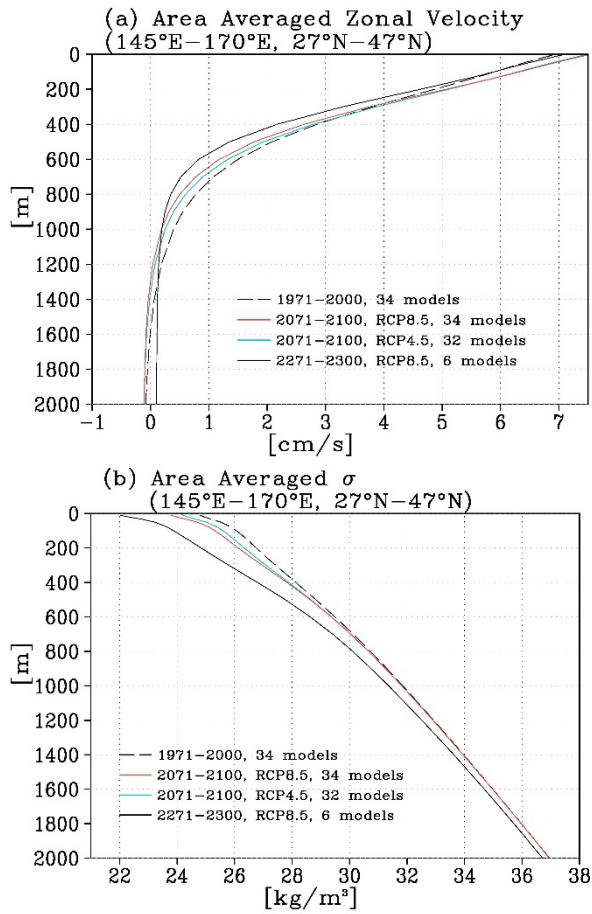
598

599 Figure 7. As in Fig. 6, but for epoch differences of KE axis latitude and DSL around the KE axis (145°–
 600 170°E, 35°–40°N) among climate models. The dashed line in (c) is the regression line from (a).



601

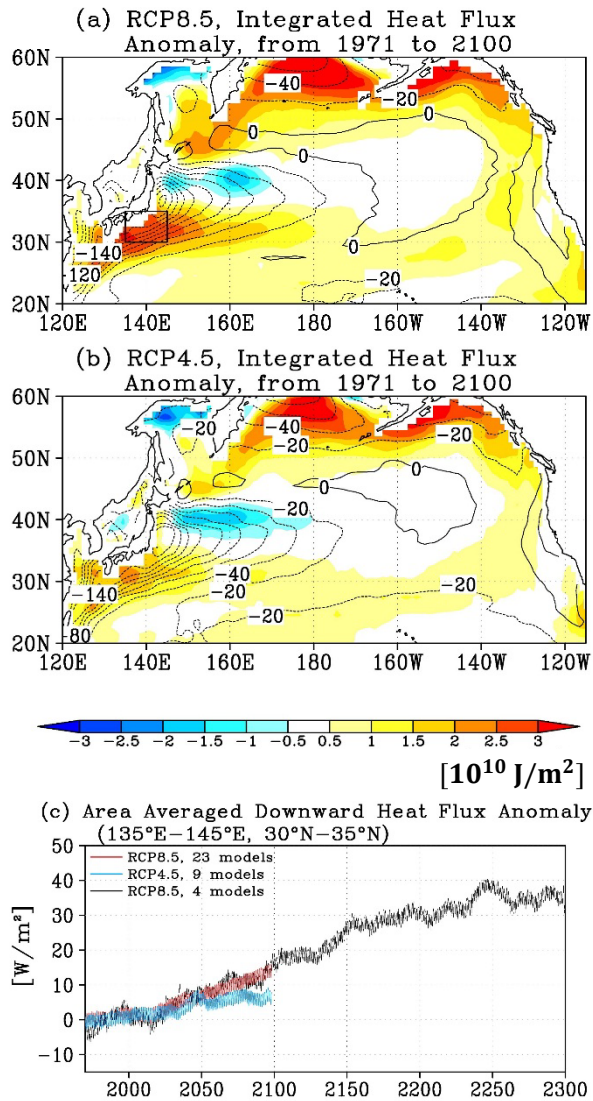
602 Figure 8. Eastward geostrophic current-speed differences (color), calculated using the zonally averaged
 603 (145°–170°E) in-situ density and sea level (a) between 1971–2000 and 2071–2100 periods for 34-model
 604 MME under RCP8.5, (b) between 2071–2100 and 2271–2300 periods for 6-model MME under RCP8.5,
 605 and (c) between 1971–2000 and 2071–2100 periods for 34-model MME under RCP4.5. Black, blue, and
 606 red contours indicate the mean zonal geostrophic current speed for the periods 1971–2000, 2071–2100,
 607 and 2271–2300, respectively.



608

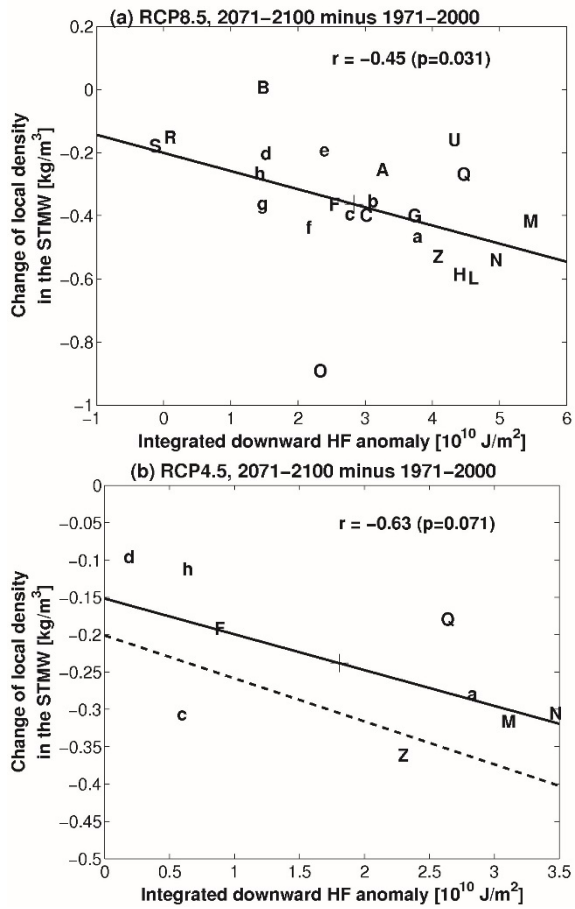
609 Figure 9. Vertical profiles of (a) zonal velocity and (b) σ averaged in 145°–170°E, 27°N–47°N for (black
 610 dashed curve) 1971–2000 period in the historical experiment, (red curve) 2071–2000 period under
 611 RCP8.5, (blue curve) 2071–2000 period under RCP4.5, and (black solid curve) 2272–2300 period under
 612 RCP8.5.

613



614
 615 Figure 10. Time-integrated downward net heat flux anomaly (color) for (a) 23-model MME under
 616 RCP8.5 and (b) 9-model MME under RCP4.5. Panel (c) shows the time series of area-averaged
 617 downward net heat flux (130°–160°E, 25°–35°N) anomaly from 1971–2000 mean smoothed by applying
 618 an 11-year running mean for the following: (red) 23-model MME under RCP8.5, (blue) 9-model MME
 619 under RCP4.5, and (black) 4-model MME under RCP8.5. Contours in panels (a) and (b) indicate the
 620 mean downward net heat flux for the period 1971–2000. The domain for area averaging is marked by the
 621 box in (a).

622



623

624

625

626

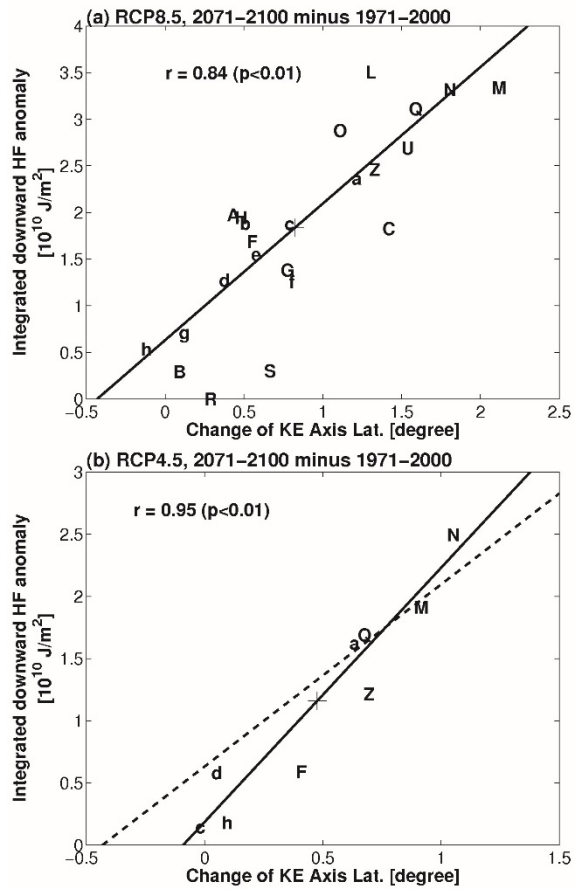
627

628

629

630

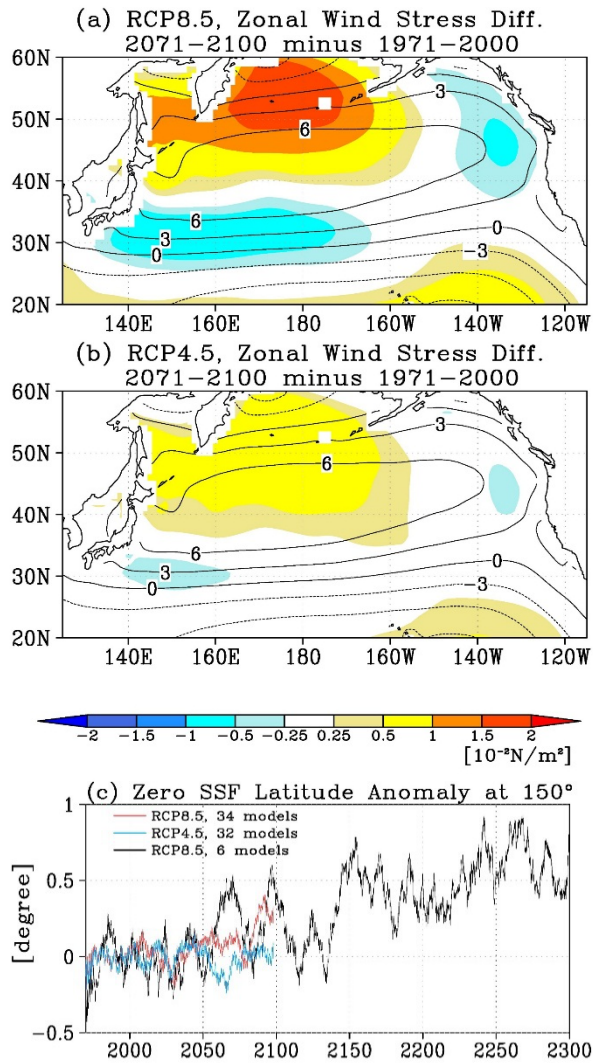
Figure 11. Scatter diagram of epoch differences of the local density averaged in the STMW region (145° – 170° E, 25° – 35° N, and depth 50–300 m) and integrated downward net heat flux averaged south of the KE (130° – 160° E, 25° – 35° N) among climate models between 1971–2000 and 2071–2100 periods. The scenarios are (a) RCP8.5 and (c) RCP4.5. The plus symbols (+) and alphabetical letters denote MME and the models (Table 1), respectively. Correlation coefficients and p -values are shown. Solid lines indicate the regression line from the data points. The dashed line in (b) is the regression line from (a).



631

632 Figure 12. As in Fig. 11, but for epoch differences of the KE-axis latitude and integrated downward net
 633 heat flux averaged south of the KE (135°–145°E, 30°–35°N) among climate models. The dashed line in
 634 (b) is the regression line from (a).

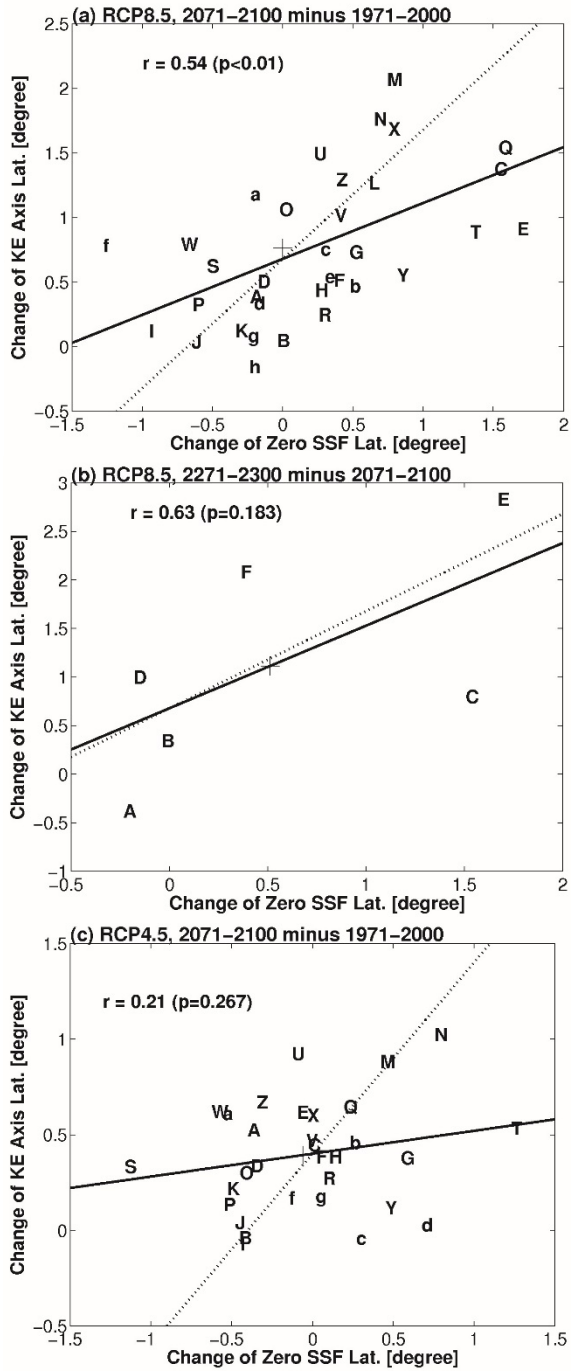
635



636

637 Figure 13. Zonal wind stress differences between 1971–2000 and 2071–2100 periods (color) (a) for
 638 34-model MME under RCP8.5 and (b) for 32-model MME under RCP4.5. Contours indicate the mean
 639 zonal wind stress for the period 1971–2000. (c) Anomaly time series of the latitude of zero SSF at 150°E
 640 relative to 1971–2000 mean smoothed by applying an 11-year running mean for the following: (red)
 641 34-model MME under RCP8.5, (blue) 32-model MME under RCP4.5, and (black) 6-model MME under
 642 RCP8.5. The zero SSF line is calculated by zonally integrating wind stress curl westward from the eastern
 643 boundary (i.e., Sverdrup Balance).

644

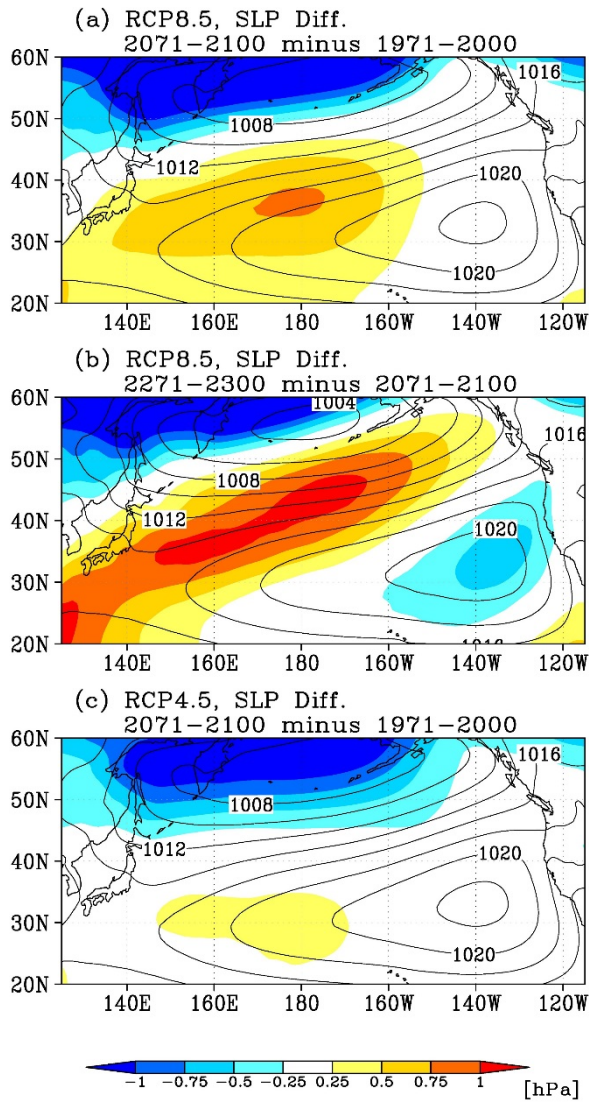


645

646

647

Figure 14. As in Fig. 6, but for epoch differences of the KE-axis latitude and the latitude of zero SSF at 150°E among climate models. Dotted lines indicate slope 1.

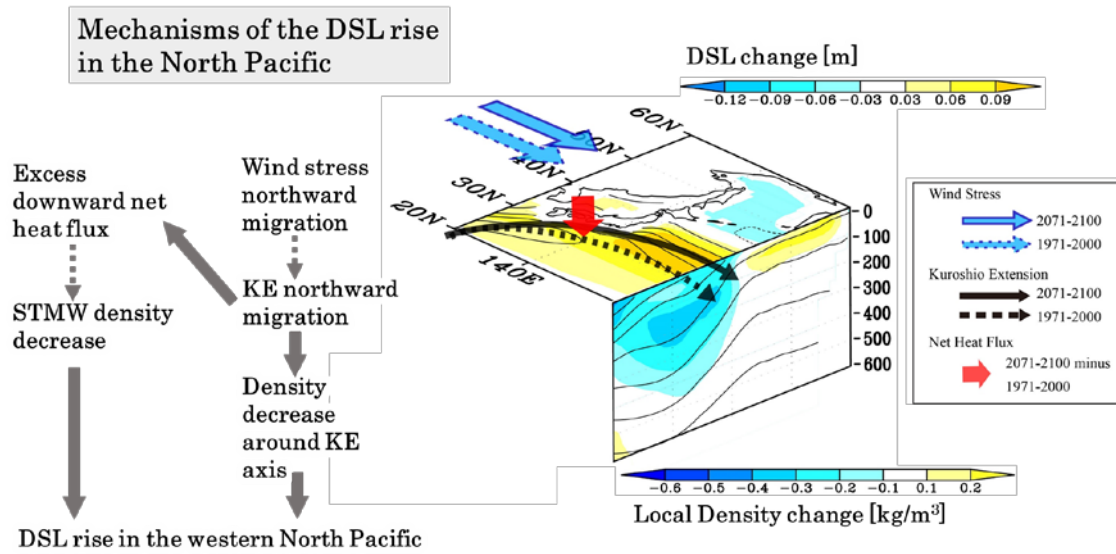


648

649 Figure 15. Epoch differences of SLP (color) (a) between 1971–2000 and 2071–2100 periods for 34-model
 650 MME under RCP8.5, (b) between 2071–2100 and 2271–2300 periods for 6-model MME under RCP8.5,
 651 and (c) between 1971–2000 and 2071–2100 periods for 32-model MME under RCP4.5. Contours indicate
 652 the mean SLP for the periods (a, c) 1971–2000 and (b) 2071–2100.

653

654



655

656 Figure 16. Schematic diagram illustrating the mechanism of DSL rise in the western North Pacific. DSL

657 rises around the KE is associated with the density decrease of the STMW and northward KE migration.

658 The STMW density decrease is caused by anomalous downward net heat flux to the south and southeast

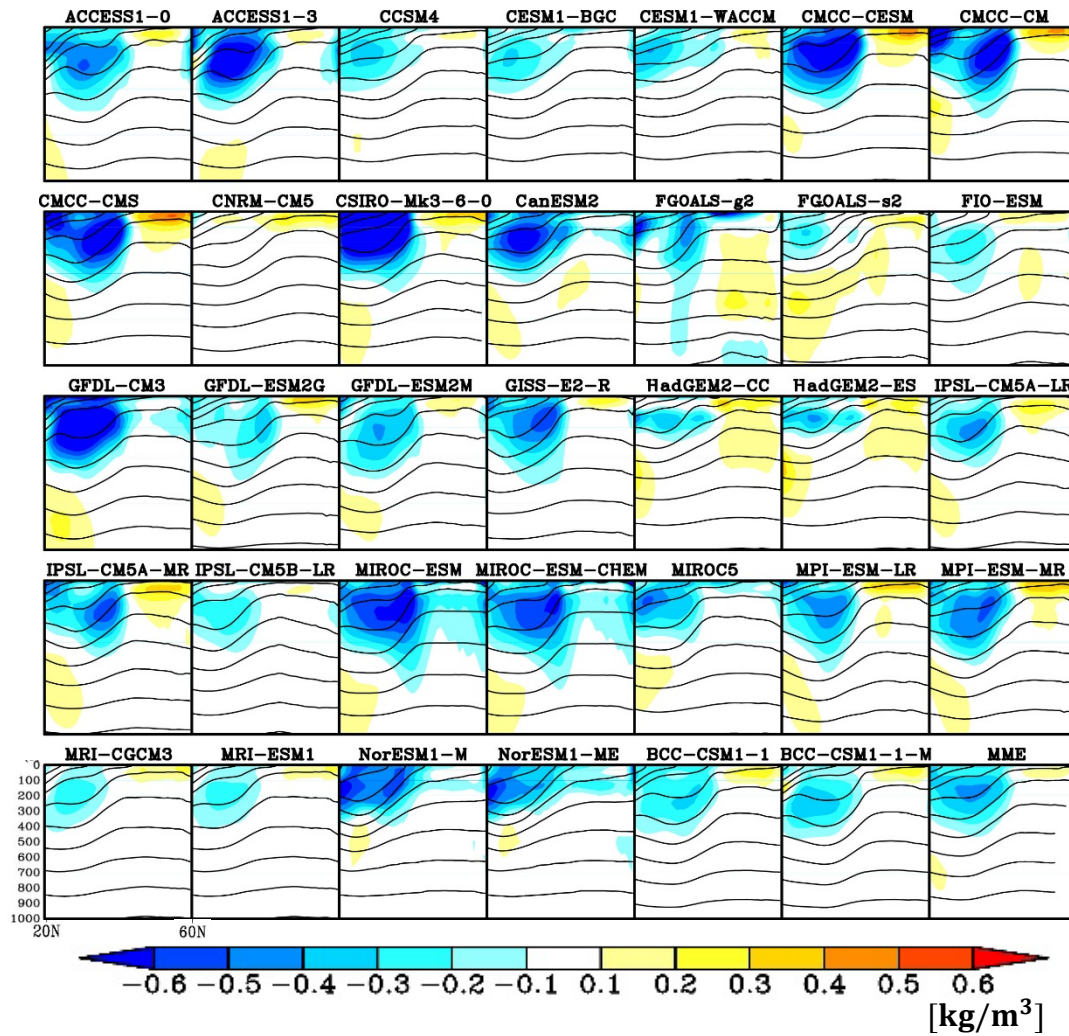
659 of Japan, while the northward KE migration is due to the poleward shift of the wind stress field. The

660 excess heat flux is also strongly related to the northward migration of the KE. The solid arrows indicate

661 the inter-model relationships that are significant at 5% significance level for both the RCP4.5 and 8.5,

662 while dashed arrows indicate the relationships that are significant only for RCP8.5 but not for RCP4.5.

663



664

665 Figure 17. Zonally averaged (145° – 170° E) local density differences between 1971–2000 and 2071–2100666 periods under RCP8.5 for each model (color). Contours indicate the mean σ for the period 1971–2000.

667 MME indicates the MME mean.

668

669